Proceedings of ASME Turbo Expo 2023
Turbomachinery Technical Conference and Exposition
GT2023
June 26-30, 2023, Boston, Massachusetts

GT2023-101212

THERMOCHEMICAL/THERMOMECHANICAL SYNERGIES IN HIGH-TEMPERATURE SOLID PARTICLE EROSION OF CMAS-EXPOSED EBCS

Jamesa L. Stokes
NASA Glenn Research Center
Cleveland, OH

Michael J. Presby
NASA Glenn Research Center
Cleveland, OH

Rebekah I. Webster
NASA Glenn Research Center
Cleveland, OH

John Setlock
University of Toledo
Toledo, OH

Bryan J. Harder
NASA Glenn Research Center
Cleveland, OH

ABSTRACT

Environmental barrier coatings (EBCs) are an enabling technology for the use of SiC-based ceramic matrix composites in next generation gas turbine engines. In the extreme engine environment, EBCs must be able to withstand a variety of individual damage mechanisms and their interactions with each other. Ingested particulates/debris can cause both thermochemical and thermomechanical degradation of EBCs. Siliceous debris primarily based on calcium magnesium aluminosilicates (CMAS) can melt and infiltrate and/or react with EBCs above 1200°C. Similarly, ingested debris can lead to mechanical damage and recession of coatings due to particulate erosion. Both modes of degradation can occur simultaneously during engine operation, and it is crucial to comprehensively understand the mechanisms of coating failure due to high-temperature particulate interactions. This study assesses the erosion durability of $Yb_2Si_2O_7$-based EBCs exposed to CMAS of various loads in NASA Glenn's Erosion Burner Rig Facility. CMAS exposures and erosion testing were carried out at 1316°C. The effects of CMAS loading and exposure time on EBC erosion durability were evaluated using Al_2O_3 as an erodent material.

This manuscript is a joint work of employees of the National Aeronautics and Space Administration and employees of the University of Toledo under Contract/Grant No. 80GRC020D0003 with the National Aeronautics and Space Administration.

Keywords: Environmental barrier coatings (EBCs); CMAS; solid particle erosion; $Yb_2Si_2O_7$; high temperature; burner rig

1. INTRODUCTION

Improvements in the efficiency of next-generation gas turbine engines have primarily been enabled by the use of SiC-based ceramic matrix composites (CMCs), which have a lower density and a higher temperature capability than traditional nickel-based superalloys. While CMCs are being implemented as hot-section engine components, they are susceptible to degradation from interactions with water vapor and other combustion products [1,2]. As such, environmental barrier coatings (EBCs) were developed to minimize the oxidation and volatilization of CMC engine components. EBCs, however, must also be able to withstand a host of damage mechanisms within the engine environment. The main damage mechanisms for EBCs include water vapor-induced volatility, thermomechanical stresses, erosion/foreign object damage (FOD), and damage due to interactions with calcium magnesium aluminosilicates (CMAS). Ultimately, predictive tools for coating failure can only be developed by understanding the interplay amongst these degradation modes.

EBC damage by CMAS has been largely attributed to both thermochemical and thermomechanical degradation mechanisms. Engine operating temperatures have increased beyond the softening/melting point of many debris compositions (>1200°C) [3–5]. Reactions at these temperatures can cause coating consumption and formation of extrinsic phases. Additionally, the infiltration of an EBC by molten deposits can cause the coating to stiffen upon cooling during thermal cycling.

This generally causes a loss in overall coating compliance as well as thermal expansion mismatches amongst the cooled melt, remaining coating, as well as any extrinsic phases present. These mismatches lead to cracking and eventual failure.

Previous solid particle erosion investigations of EBCs focused on the effects of impingement angle, particle kinetic energy, and surface roughness on the mechanical removal of coating material due to particle impacts [6]. However, the erosive performance of these materials after exposure to CMAS has not been studied. CMAS exposure causes significant microstructural transformation of EBCs that will likely influence the mechanical durability of these coatings. Determination of the implications of damage mechanism synergies are crucial to understanding the service lifetime of current and future EBC systems.

In this work, we present initial results on evaluating the erosion resistance of CMAS-exposed coatings at high temperature. This study forms a basis for future testing methodologies and design strategies used to evaluate synergistic damage mechanisms in EBCs due to particle interactions in an engine-like environment.

2. MATERIALS AND METHODS

The coating used in this work was a ytterbium disilicate ($Yb_2Si_2O_7$, YbDS) topcoat modified with additions of 1.39 wt.% mullite ($3Al_2O_3 \cdot 2SiO_2$) and 2.33 wt.% yttrium aluminum garnet ($Y_3Al_5O_{12}$) for improved bondcoat (BC) oxidation performance [7]. The modified $Yb_2Si_2O_7$ topcoat (hence referred to as M2Y in this paper) along with a Si bondcoat were deposited via air plasma spray onto 25.4 mm diameter by 3 mm thick SiC Hexoloy® SA monolithic substrates. The target thickness of the topcoat and bondcoat was ~250 µm and ~100 µm, respectively. Deposition parameters of the bondcoat and topcoat are proprietary to NASA. An exemplary image of the as-deposited microstructure of the coatings is shown in Figure 1.

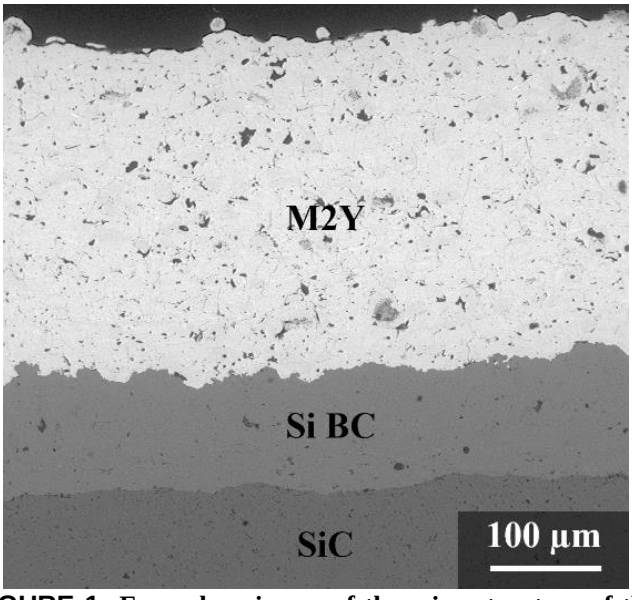

FIGURE 1: Exemplary image of the microstructure of the as-received coatings.

$CaCO_3$ (>99.0%, Alfa Aesar), MgO (99.95%, Cerac Inc.), Al_2O_3 (>99.0%, Almatis Inc.), and SiO_2 (99.5%, Alfa Aesar) were used as the starting powders to prepare a CMAS glass; procedures outlined in the authors' previous CMAS investigations were utilized [8,9]. A nominal composition of $30.67CaO - 8.25MgO - 12.81AlO_{1.5} - 48.27SiO_2$ was chosen for this study, being roughly equal to deposits observed on aircraft shrouds impacted by desert sand [10,11] and also used as a standard CMAS composition across several studies. Five different loading values were investigated in this paper: ~2, ~4, ~6, ~18, and ~36 mg/cm^2. In the ~2 mg/cm^2 and ~4 mg/cm^2 samples, CMAS was applied via air brush [12]. In the ~6 mg/cm^2, ~18 mg/cm^2, and ~36 mg/cm^2 samples, CMAS tapes were stacked on the surfaces of the coatings. Tapes were cast from a slurry made from this CMAS composition using methods comparable to those developed in a previous paper [13]. Two different tape loadings were produced, being ~6.3 mg/cm^2 and ~8.9 mg/cm^2. Circles of 9.53 mm diameter (~37% of the sample diameter) were punched out of the CMAS tapes and stacked to their respective loadings on the coating surfaces. A single layer of the ~6.3 mg/cm^2 tape was used for the ~6 mg/cm^2 samples. Two and four layers of the ~8.9 mg/cm^2 tape were used for the ~18 mg/cm^2 and ~36 mg/cm^2 samples, respectively. The samples stacked with tapes were then heated to 420°C at 0.2°C/min, held for 2 hours, then cooled to room temperature at 2°C/min to burn off any organics in the tapes. The CMAS-loaded samples were all heat treated in a stagnant-air box furnace at 1316°C for 4 hours, with select samples undergoing additional heat treatment at 1316°C for 100 hours. All samples were heated and cooled at 10°C/min after the initial organic burnout.

Erosion experiments were conducted using a modified NASA Glenn Research Center Mach 0.3 to Mach 1.0 burner rig that operates on Jet-A fuel and pre-heated air [6,14–17]. Erodent is injected into the burner chamber using a screw-driven powder feeder (HA 5000F-SA, Hardface Alloys, Inc.) where it then passes through a 19 mm exit nozzle, and accelerates downstream through a 19 mm diameter, 305 mm long unattached duct to the sample. An Inconel® 601 clamshell fixture is used to hold the sample during testing. The sample was placed at a standoff distance of 30 mm with respect to the duct exit. Samples were heated to 1316°C (~2400°F) as measured by an Ircon Modline 7.9 µm single-color pyrometer. After reaching the target temperature, samples were exposed to ~60 µm alumina (Al_2O_3) particles (Treibacher Schleifmittel, GmbH) that were fed into the burner at a rate of 2 g/min. Alumina (Al_2O_3) was chosen as the erodent (Figure 2) because it is readily available and shown to produce erosion "scars" or damage similar to that observed in engine hardware [16–18]. The particles were very sharp and angular (Figure 2(a)). Particle size analysis carried out on a MicroTrac Sync analyzer (MicroTrac MRB, York, PA) indicated that the particles had an average size of 63.92 µm, with a 25.97 µm standard deviation (Figure 2(b)).

The particle velocity was measured to be 135 m/s using a high-temperature double-disk velocimeter [19–22]. The angle of particle impingement, α, was fixed at 90°. One sample was eroded at each loading condition. Samples were subjected to

multiple exposures of 30 s each (1 g of erodent) where the sample mass was measured before and after each successive exposure using a scale with precision of 0.01 mg. A total of 10 exposures equating to a cumulative exposure of 10 g of erodent was used. The effective area of erosion on the sample was roughly the same width as the unattached duct (19 mm, ~75% of coating surface area).

The microstructure and composition of reaction products formed in the CMAS-exposed samples were determined using scanning electron microscopy (SEM, Hitachi S4700 FESEM) and energy dispersive spectroscopy (EDS, Oxford Instruments), respectively, before and after erosion. Optical profilometry images (Keyence VR-3200 3D Measurement Microscope) were taken of select samples at points throughout the erosion testing to track surface morphology evolution as a function of cumulative erodent used.

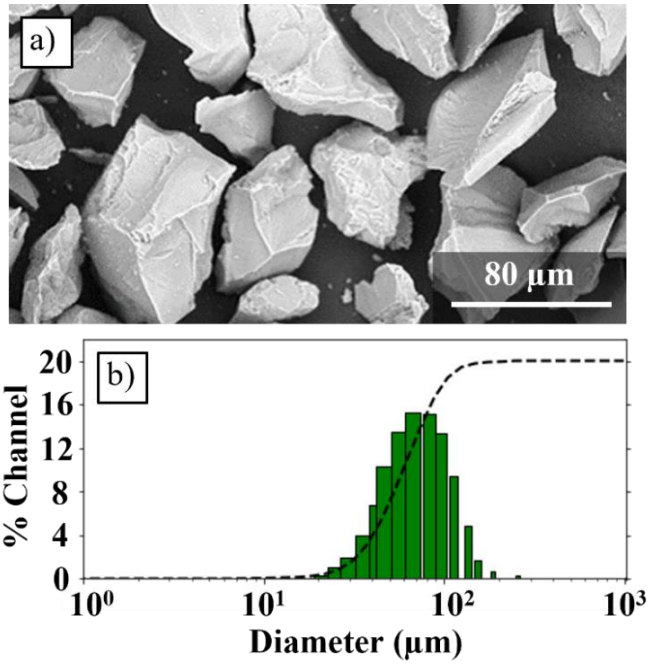

FIGURE 2: a) Micrograph of the Al_2O_3 erodent particles. b) Particle size distribution plot of Al_2O_3 erodent.

3. RESULTS AND DISCUSSION

3.1 ~2 mg/cm² and ~4 mg/cm² CMAS Loaded Samples

Figures 3(a,b) and (c) display a non-eroded coating surface and bondcoat interface after exposure to ~4 mg/cm^2 CMAS for 4 hours at 1316°C, respectively. The morphology of the samples exposed to ~2 mg/cm^2 and ~4 mg/cm^2 CMAS were similar. No residual CMAS was observed on the surface of either sample after exposure. The higher magnification image of the coating surface shown in Figure 3(b) indicates that the interaction region consisted of pockets of CMAS interspersed with elongated grains having a composition consistent with that of $Ca_2Yb_8(SiO_4)_6O_2$ apatite, a crystalline phase typically expected to form between EBCs and CMAS of various compositions [23–26].

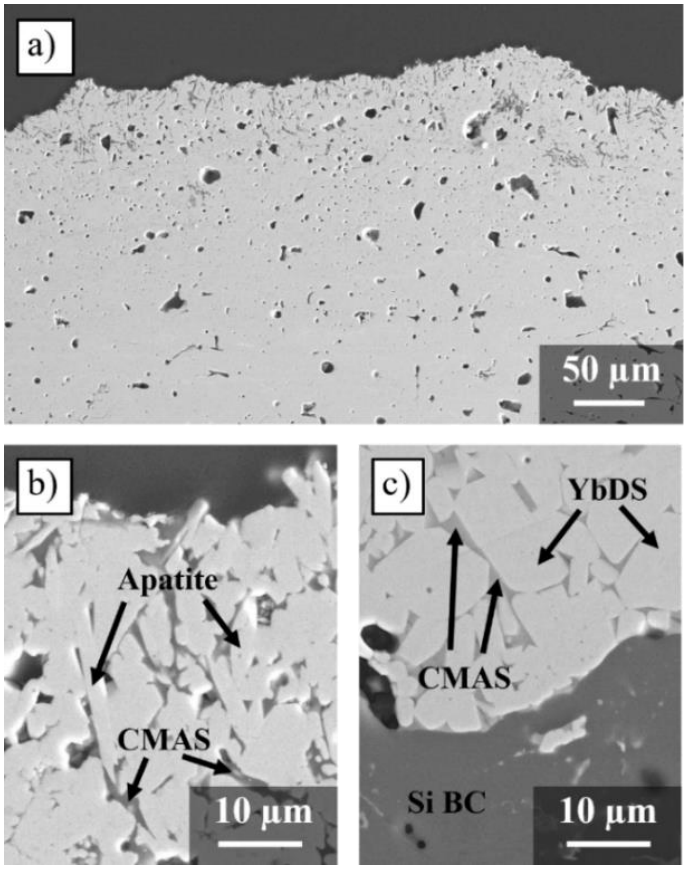

FIGURE 3: a) Micrograph of ~4 mg/cm^2, 4 hours sample with b) higher magnification image of CMAS reaction layer at the surface and c) pockets of CMAS between YbDS grains at the bondcoat interface.

In both loading cases, the thickness of this region was measured to be ~40 µm; the microstructure of the topcoat appeared fairly dense throughout. Pockets of CMAS were also observed near the bondcoat, as shown in Figure 3(c). The total thickness of the YbDS coating after exposure to ~2 and 4 mg/cm^2 CMAS was comparable to the starting thickness of the as-received coatings, suggesting that any interaction with CMAS did not result in a change of coating thickness or volume.

3.1.1 Erosion after ~2 mg/cm² and ~4 mg/cm² CMAS Exposure

Figure 4 shows the erosion of the coatings before and after exposure to ~2 and ~4 mg/cm^2 CMAS. With increasing CMAS load, the cumulative mass loss decreased slightly in magnitude. The cumulative mass loss versus cumulative erodent curve for the as-received sample exhibited fairly linear behavior throughout the entire test. The CMAS-exposed samples exhibited some initial non-linearity before reaching a more well-defined linear region. In previous erosion studies of CMCs and EBCs, the well-defined linear region was used to represent "steady-state" erosion behavior [6]. For consistency, the steady-state erosion rate was taken as the slope of the last six points of the erosion curves. The erosion rates of the as-received coating,

~2 mg/cm^2, 4 hour and ~4 mg/cm^2, 4 hour samples were estimated to be 16.34 mg/g, 16.08 mg/g and 16.43 mg/g, respectively. The effective steady state erosion rates of the ~2 and ~4 mg/cm^2 samples were roughly equal to that of the unexposed coating. Hence, at these low loadings, it appears that CMAS interaction did not negatively affect erosion resistance. The as-received coating contained ~8% porosity as determined by image analysis, whereas the ~2 mg/cm^2, 4 hour and ~4 mg/cm^2, 4 hour samples had ~6% and ~5% porosity, respectively. While this change in coating microstructure is minimal, some densification of the material could have resulted in the lower cumulative mass loss of the CMAS-exposed coatings.

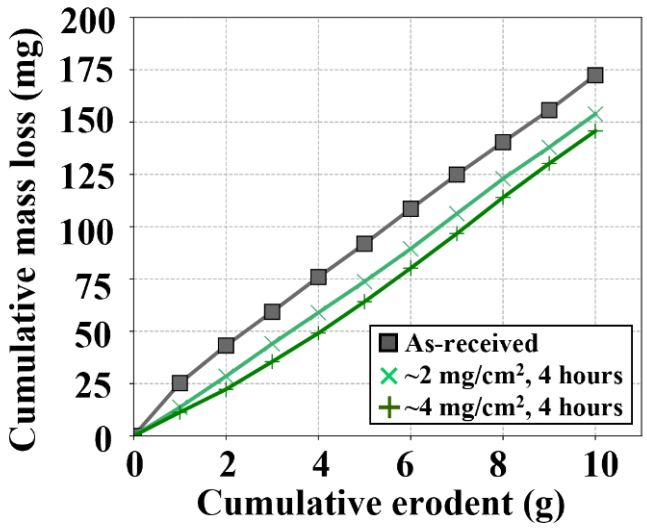

FIGURE 4: Cumulative mass loss vs cumulative erodent of the as-received, ~2 mg/cm^2, 4 hours and ~4 mg/cm^2, 4 hour samples.

3.2 ~6 mg/cm^2, ~18 mg/cm^2, and ~36 mg/cm^2 CMAS Loaded Samples

Figure 5 shows optical images of samples after exposure to CMAS at 1316°C, with inset color maps from profilometry measurements also displayed. For the sample exposed to ~6 mg/cm^2 CMAS for 4 hours (Figure 5(a)), there was little CMAS remaining on the surface. However, both the ~18 mg/cm^2, 4 hour and ~36 mg/cm^2, 4 hour samples (Figure 5(b) and Figure 5(c), respectively) showed larger residual bubbles of molten CMAS. After 100 hours, the coating surface area of CMAS infiltration in the ~6 mg/cm^2 sample (Figure 5(d)) did not appear to expand further than the original area of the deposited CMAS tape. Both the ~18 mg/cm^2, 100 hour (Figure 5(e)) and ~36 mg/cm^2, 100 hour (Figure 5(f)) samples exhibited bubbling and rumpling of the coating; the change in coating morphology was more severe for the ~36 mg/cm^2 sample. The deposited CMAS appeared to have interacted with the entirety of the coating in the ~36 mg/cm^2, 100 hour sample. The observed bubbling and rumpling suggest that the coating underwent volumetric changes due to possible extrinsic phase formation as well as glass infiltration. SEM images of the CMAS interaction zones are displayed in Figure 6. The morphology of the interaction zones as a function of CMAS loading appeared very similar after 4 hours. A thin, darker phase was observed within the residual CMAS in each sample, as shown in Figures 6(a), (c), and (e), and identified as anorthite via EDS ($CaAl_2Si_2O_8$) that crystallized from the residual melt.

Like the ~2 and ~4 mg/cm^2, 4 hour samples, elongated $Ca_2Yb_8(SiO_4)_6O_2$ apatite needles were observed near the coating surface in the ~6, ~18 and ~36 mg/cm^2, 4 hour samples; however, the precipitates appeared much larger. From the surface to about two-thirds of the thickness of the coating, CMAS was observed between the precipitates. Below this depth, the remaining YbDS appeared to be denser near the bondcoat interface. Apatite grains were mostly concentrated near the surface of the coatings. Below the apatite-rich surface region, apatite grains appeared to become increasingly interspersed with YbDS grains as a function of depth before trailing off into the densified YbDS layer. Vertical cracks were also observed going through the residual CMAS and the coatings, which could be the result of thermal expansion mismatch between the various phases present after CMAS exposure. For all samples, the YbDS region near the bondcoat appeared less dense after 100 hours, with CMAS pockets interspersed between YbDS grains.

The apatite and YbDS grains seemed to have coarsened in the ~18 mg/cm^2 and ~36 mg/cm^2 samples after 100 hours (Figure 6(d) and Figure 6(f), respectively). In the ~6 mg/cm^2, 100 hour sample (Figure 6(b)), most of the larger apatite grains were no longer present, although very small apatite precipitates were observed in some CMAS pockets at the surface. Regions of locally dense YbDS were still present in the ~6 mg/cm^2, 100 hour sample. No dense regions of YbDS remained in the ~18 mg/cm^2 and ~36 mg/cm^2 samples after 100 hours.

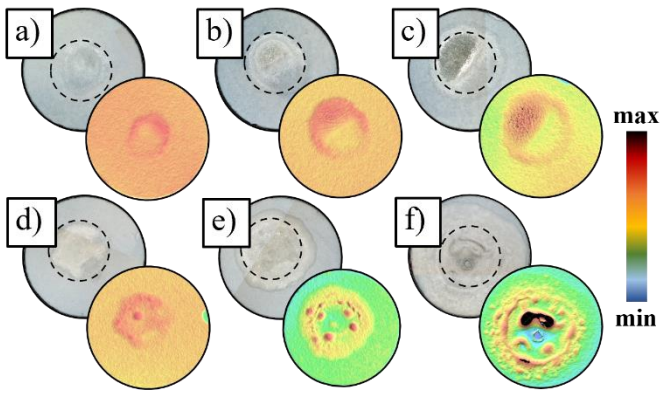

FIGURE 5: Optical images of the a) ~6 mg/cm^2, 4 hour, b) ~18 mg/cm^2, 4 hour, c) ~36 mg/cm^2, 4 hour, d) ~6 mg/cm^2, 100 hour, e) ~18 mg/cm^2, 100 hour, and f) ~36 mg/cm^2, 100 hour samples with inset color maps from profilometry to further demonstrate differences in surface morphology. The color bar shows maximum and minimum relative height. The dashed circles indicate the original area of the CMAS tapes placed on the EBC surfaces before heat treatment. Samples are 1 in. in diameter.

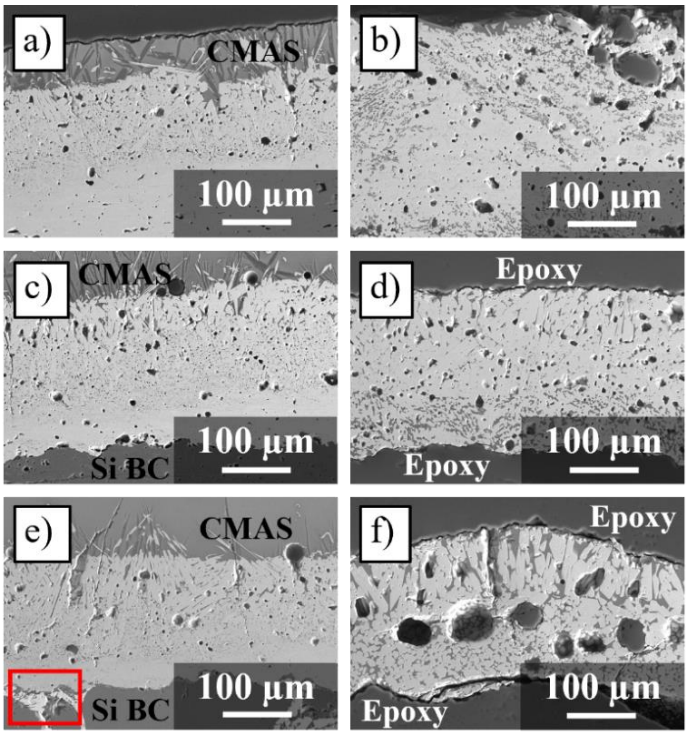

FIGURE 6: SEM micrographs of CMAS interaction regions observed in the a) ~6 mg/cm^2, 4 hour, b) ~6 mg/cm^2, 100 hour, c) ~18 mg/cm^2, 4 hour, d) ~18 mg/cm^2, 100 hour, e) ~36 mg/cm^2, 4 hour, and f) ~36 mg/cm^2, 100 hour samples. The red box shows region of platinum deposited on the sample from a faulty sputtering mechanism.

There was a bright phase observed within the bond coat in the ~36 mg/cm^2, 4 hour sample, as highlighted by the red box in Figure 6(e). From compositional analysis via EDS, it was determined that this bright phase was one of several deposits of platinum that had been traced back to a faulty sputtering mechanism when coating the sample to reduce charging in the electron microscope.

SEM images of the bondcoat interface are displayed in Figure 7 for each sample. Small pockets of CMAS were observed near the bond coat in all samples, as was also seen in the ~2 and ~4 mg/cm^2 samples, indicating that CMAS completely infiltrated the coatings for all loadings. The interface between the coating and bondcoat was similar for all samples after 4 hours of exposure, with small voids beginning to form at this interface. Larger voids were observed to form in the ~6 mg/cm^2 sample after 100 hours of exposure, as shown in Figure 7(b). In both the ~18 mg/cm^2 and ~36 mg/cm^2 samples (Figure 7(d) and Figure 7(f), respectively), the coatings delaminated in large sections from the bondcoat after 100 hours. It was evident that coating delamination occurred after CMAS infiltration of the coatings, while CMAS-affected regions were still attached to the bondcoat. Both the formation of voids and observation of CMAS between YbDS grains suggests that CMAS infiltration occurred via grain boundaries in the coating.

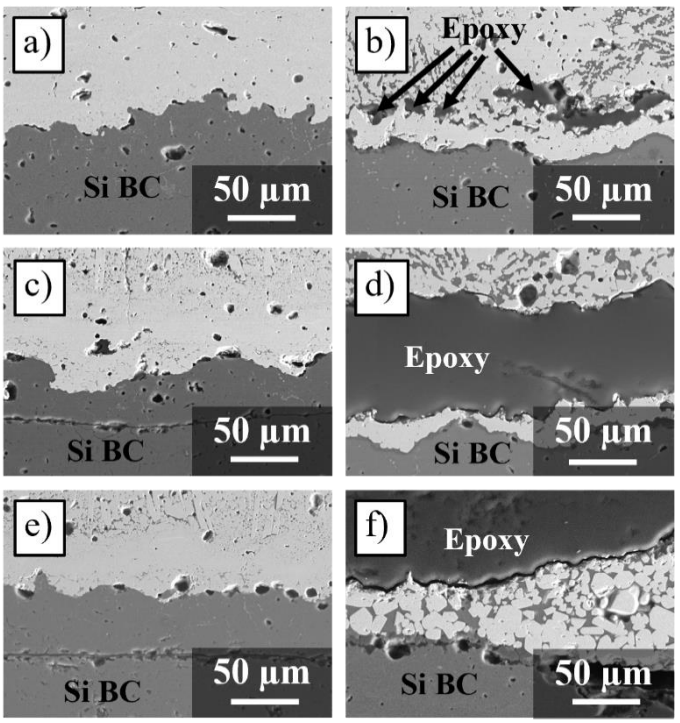

FIGURE 7: SEM micrographs of the coating/ bondcoat interface in the a) ~6 mg/cm^2, 4 hour, b) ~6 mg/cm^2, 100 hour, c) ~18 mg/cm^2, 4 hour, d) ~18 mg/cm^2, 100 hour, e) ~36 mg/cm^2, 4 hour, and f) ~36 mg/cm^2, 100 hour samples.

Such large voids were hypothesized to form in response to swelling of the coating material caused by grain boundary ingress, as has been documented in previous studies [27–29]. While there was evidence that CMAS infiltrated the coating down to the bondcoat, there was no indication that CMAS had reacted with or infiltrated the Si bondcoat after either 4 or 100 hours.

3.2.1 Erosion after ~6 mg/cm^2, ~18 mg/cm^2 and ~36 mg/cm^2 CMAS Exposure

Figure 8 displays erosion plots for the ~6 mg/cm^2, 4 hour, ~18 mg/cm^2, 4 hour, and ~36 mg/cm^2, 4 hour samples. With increasing CMAS load (up to ~18 mg/cm^2), the cumulative mass loss decreased with increasing cumulative erodent. The ~36 mg/cm^2 sample exhibited an initial mass gain up to approximately 3 g of cumulative erodent followed by mass loss. An optical image of the 36 mg/cm^2 sample is displayed in Figure 9 along with SEM surface analysis of the residual CMAS bubble after erosion with 1 g of Al_2O_3. Micrographs of the sample (Figure 9(a)) indicated that large particulates were embedded in the residual CMAS on the surface. EDS analysis (Figure 9(b)) showed that these particulates were Al-rich, indicating that the Al_2O_3 erodent was embedding into the residual CMAS. This result suggests that erodent particles were more likely to become embedded in the residual CMAS when there was a considerable amount of CMAS remaining on the coating surface, as was the case for the ~36 mg/cm^2, 4 hour sample.

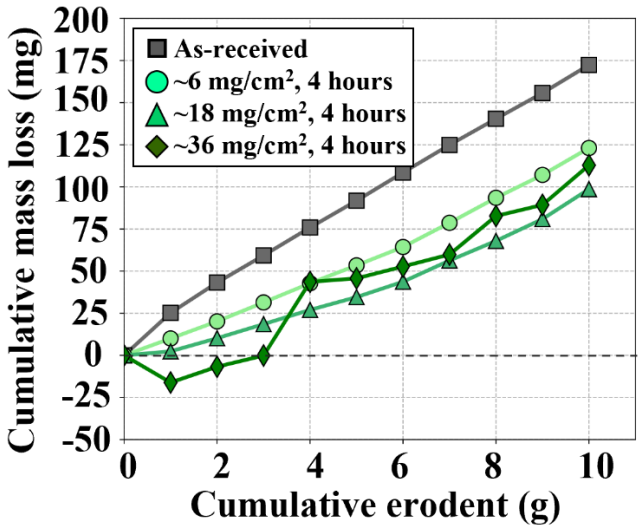

FIGURE 8: Cumulative mass loss vs cumulative erodent for the as-received, ~6 mg/cm², 4 hour, ~18 mg/cm², 4 hour and ~36 mg/cm², 4 hour samples.

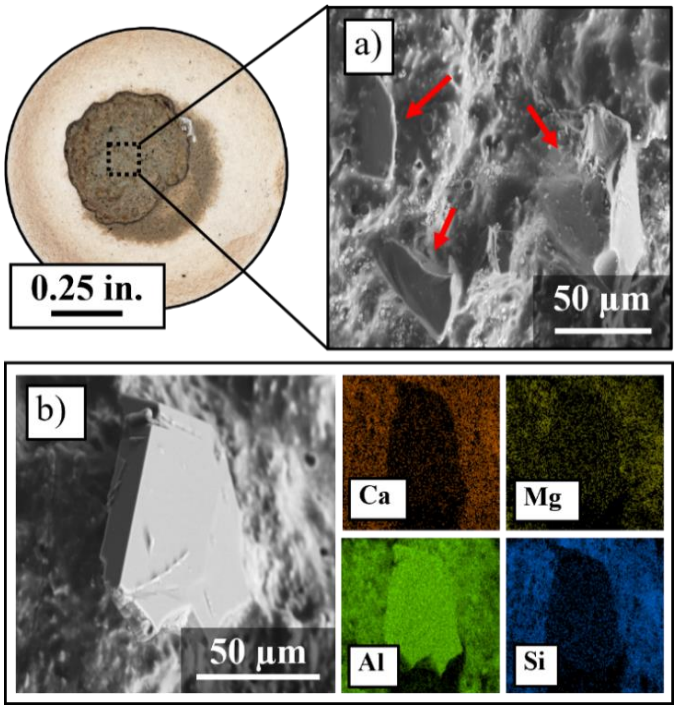

FIGURE 9: Optical image of the partially eroded ~36 mg/cm², 4 hour sample with a) SEM micrograph of Al_2O_3 erodent particles (indicated by the red arrows) embedded in residual CMAS on the EBC surface and b) higher magnification micrograph of an Al_2O_3 particle with corresponding EDS element maps.

A negative mass loss indicated that the rate of particulate accumulation was higher than the rate of erosion of surrounding material. The accumulation of erodent in the CMAS-exposed samples could also explain the early non-linear behavior of mass loss for both the ~6 mg/cm² and ~18 mg/cm² samples. Although the presence of residual CMAS with increasing load seemed to result in some mass gain, the overall steady-state rate of mass loss (i.e., the slope of the last six data points) appeared similar regardless of CMAS loading. While the last six points are not linear, an approximation of a linear slope for the ~6, ~18 and ~36 mg/cm² loaded samples resulted in erosion rates of 14.05 mg/g, 12.68 mg/g, and 13.38 mg/g, respectively, all being slightly less than the as-received and lower loading samples.

At 4 g of erodent used (4th data point), the ~36 mg/cm² sample exhibited a sharp increase in mass loss; this was followed by much smaller changes in mass up to 10 g. Optical images and profilometry measurements of all samples at select erodent amounts are displayed in Figure 10. There were no substantial changes in the surface morphology of the ~6 mg/cm² sample throughout the entire erosion test. In the ~18 mg/cm² sample, residual CMAS on the surface of the coating appeared to bubble and rumple from high-temperature exposure in the burner rig. Similar bubbling was also observed in the ~36 mg/cm² sample up to 3 g of exposure. At 4 g, it was observed that a large piece of the residual CMAS bubble in the ~36 mg/cm² sample broke off during testing, which probably contributed to the substantial increase in measured mass loss at this amount of cumulative erodent (Figure 8).

While higher CMAS loads seemed to reduce the overall mass loss after 4 hours CMAS exposure, CMAS exposure for 100 hours (Figure 11) resulted in immediate catastrophic failure of the ~18 mg/cm² (Figure 11(b)) and ~36 mg/cm² (Figure 11(c)) samples when heated by the burner rig to start the erosion test and were therefore not eroded. Compositional analysis of the regions of delamination indicated that the bondcoat was still mostly attached to the substrate, meaning that coating failure occurred at the topcoat/bondcoat interface. Erosion testing was completed for the ~6 mg/cm², 100 hour sample (Figure 11(a)), and its erosion behavior is plotted with the ~6 mg/cm², 4 hour sample in Figure 12. Cumulative mass loss in the ~6 mg/cm², 100 hour sample was higher than that in the ~6 mg/cm², 4 hour sample and comparable to that in the as-received sample during the first half of the erosion test. After 4 g, the cumulative mass loss of the ~6 mg/cm², 100 hour sample decreased, becoming lower than that of the as-received sample but still slightly higher than that of the 4 hour sample.

As shown in Figure 6(b), a longer heat treatment resulted in the formation of voids in the ~6 mg/cm² coating. The formation of these defects may negate the benefits to erosion durability possibly caused by densification of the coating due to viscous sintering from CMAS exposure, which may explain the similar erosion rate to that of the as-deposited coating in the first half of the test (The slope of the first six points resulted in an erosion rate of 15.60 mg/g). However, the lower erosion rate in the second half of the test (12.34 mg/g) could indicate that denser regions of the coating were being eroded, as microscopy indicated the majority of the voids were concentrated towards the surface. Hence, in the second half of the erosion test, the lower cumulative mass loss trend could be the result of eroding past the porous regions in this coating.

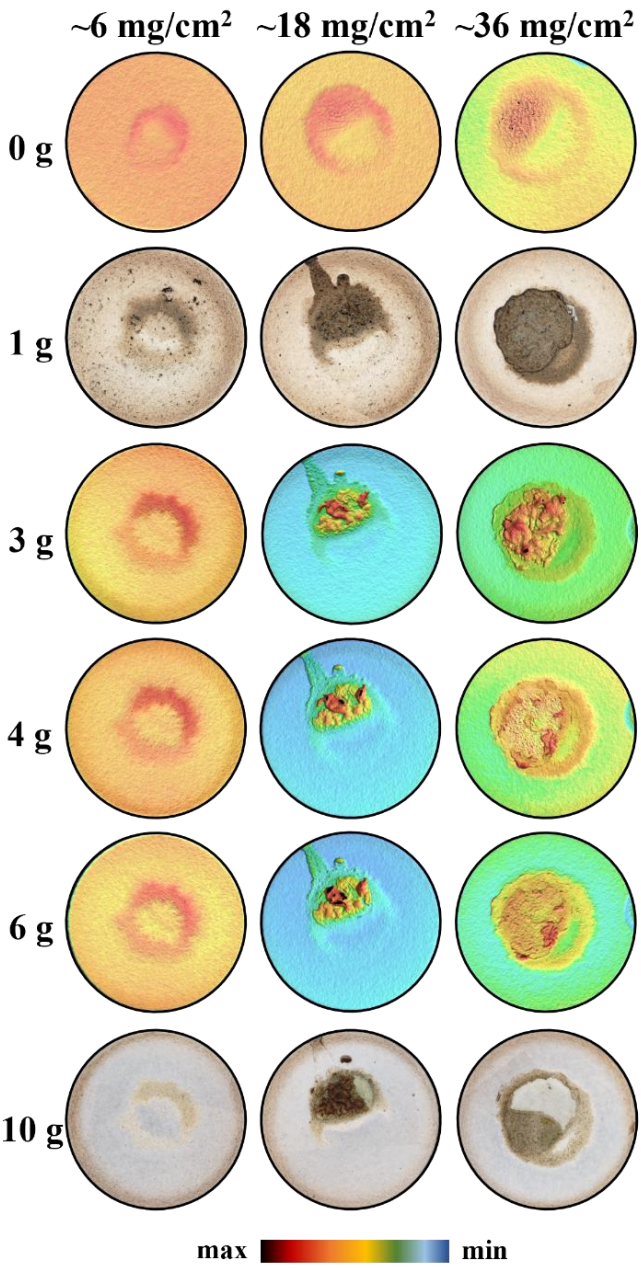

FIGURE 10: Optical images/profilometry color maps obtained during erosion testing of the ~6 mg/cm², 4 hour, ~18 mg/cm², 4 hour, and ~36 mg/cm², 4 hour samples. The color bar shows maximum and minimum relative height. Samples are 1 in. in diameter.

3.3 Implications on EBC Durability

At low loadings (~2-4 mg/cm²), there were minimal changes in the erosion rates when compared to an as-received coating. Overall, the cumulative mass loss decreased with increasing CMAS load although the steady-state rates were effectively unchanged. Erosion testing of samples exposed to CMAS for 4 hours indicated that there may be some benefit of CMAS exposure to the mechanical durability of the M2Y coating. At low loadings, the introduction of a glassy phase could aid in the densification/viscous sintering of these coatings during heat treatment, improving the mechanical strength of this material.

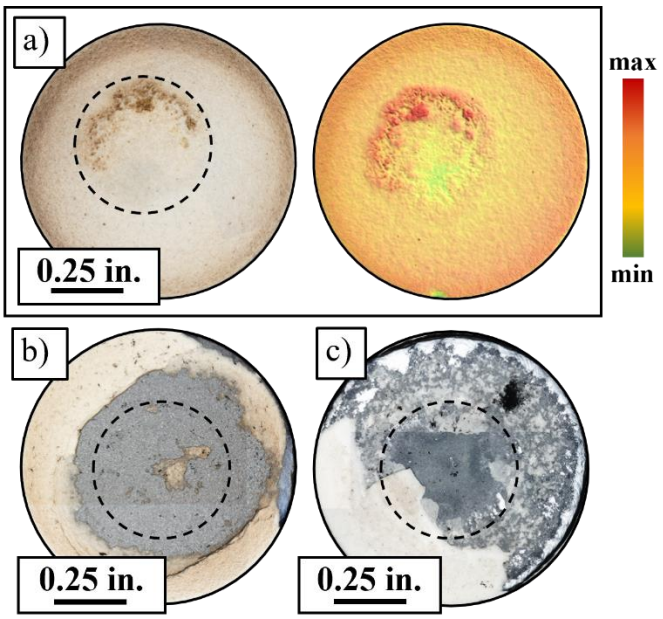

FIGURE 11: a) ~6 mg/cm², 100 hour sample after erosion testing at 1316°C with corresponding profilometry color map. b) ~18 mg/cm², 100 hour sample after immediate exposure to the burner rig torch. c) ~36 mg/cm², 100 hour sample after immediate exposure to the burner rig torch. The dashed circles indicate the original areas of the CMAS tapes placed on the EBC surfaces prior to heat treatment. The color bar shows maximum and minimum relative height.

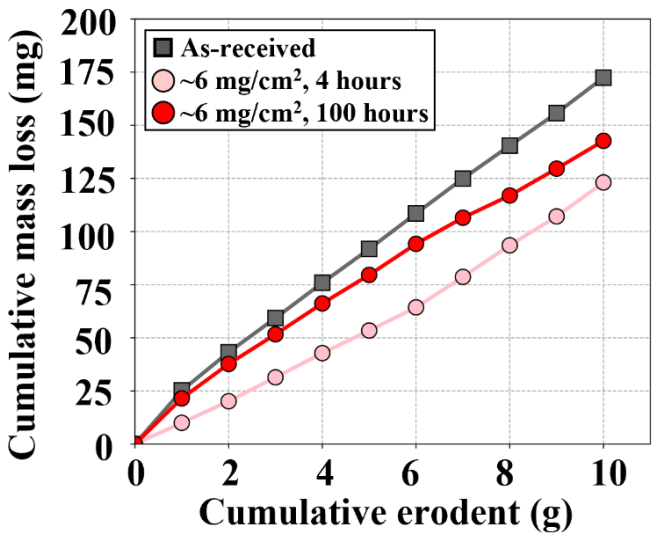

FIGURE 12: Cumulative mass loss vs cumulative erodent for the as-received, ~6 mg/cm², 4 hour, and ~6 mg/cm², 100 hour samples.

Additionally, molten glass can flow and fill pores and lamellar cracks that arise during the deposition process, thus reducing defect centers that can propagate cracks due to particle impacts. However, densification could also result in loss of compliance of coating and other unfavorable consequences to coating integrity that have not been covered in this investigation. Initially, heat treatment of the ~6 mg/cm^2, ~18 mg/cm^2, and ~36 mg/cm^2 samples for 4 hours and subsequent erosion testing also indicated some advantage of CMAS exposure to the mechanical durability of these EBCs exposed to higher CMAS loads; nevertheless, additional analyses revealed greater changes in the coating chemistry and morphology, which are not captured in mass loss plots and could be detrimental to the coatings in service.

Mass gain was observed as loading increased (Figure 8), which was caused by Al_2O_3 particles impinging and becoming embedded within the residual CMAS. This effect was most evident in the ~36 mg/cm^2 sample heat treated for 4 hours. Optical images and profilometry maps (Figure 10) showed that the coating surrounding the CMAS bubble was thinner, indicating that while the Al_2O_3 particles were sticking to the residual CMAS, particle impacts were still removing material in the surrounding areas not covered by CMAS (the CMAS affected area was roughly equal to the starting tape diameter (9.53 mm), being smaller than the effective eroded area (19 mm)). The Al_2O_3 particles observed in residual CMAS were of similar size to the starting erodent particle size (Figure 9(b)), suggesting that the majority of the Al_2O_3 particles did not become molten during testing.

It is important to note that while the sample temperature was measured to be 1316°C, it was unclear as to whether the Al_2O_3 particles reached testing temperature. In application, it is expected that CMAS particles impinging on a surface will have much lower melting points than the Al_2O_3 erodent used in this study. Thus, CMAS particles are more likely to "splat" and stick to coatings than to remove material, resulting in even less material loss than what was observed here. Conversely, it has been computationally demonstrated that larger particles of CMAS (>40 µm) do not necessarily fully melt in burner rig tests [30]. Hence, impingement of partially molten CMAS particles may result in simultaneous erosive removal and adhesion to coating materials. Similarly, fluid dynamics calculations as those done by *Kuczmarski et al.* on CMAS powders during burner rig testing may also shed light into the behavior of Al_2O_3 particles in the torch during testing for future studies [15].

As mass accumulates on the surface, large chunks of material can also break away from the coating, as demonstrated by the loss of the residual CMAS bubble in the ~36 mg/cm^2 sample heat treated for 4 hours. Figure 13 shows facets of coating damage that were apparent after erosion testing. Additional vertical cracks, embedded Al_2O_3 particles, early void formation at the bondcoat interface, and extensive crack widening in the bondcoat were all observed. The spallation of the CMAS bubble was likely the combination of thermal shock as the sample was rotated into the burner rig torch for testing and possible stresses caused by thermal expansion mismatches among CMAS, YbDS,

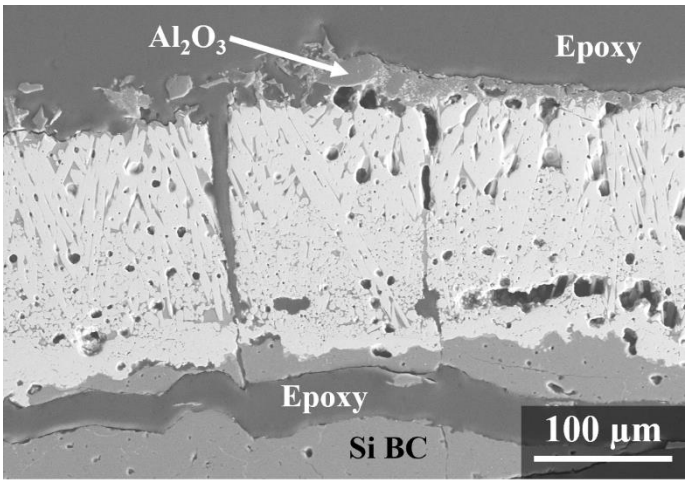

FIGURE 13: SEM micrograph of the ~36 mg/cm^2, 4 hour sample after erosion testing.

and extrinsic phases like apatite. In addition to thermal expansion mismatch issues, differences in the mechanical properties of the reaction products (residual CMAS, apatite, YbDS, anorthite, etc.) could contribute to the durability of the coating as a whole, as evidenced by the non-linear erosion behavior observed during testing, which could be indicative of a changing erosion rate. The fracture toughness of some CMAS glasses and mineral phases like anorthite has been estimated to be ~0.7-0.75 MPa·m$^{1/2}$ [5,31,32], while the fracture toughness of YbDS was determined to be ~2 MPa·m$^{1/2}$ [33]. The mechanical properties of $Ca_2RE_8(SiO_4)_6O_2$ materials have not been studied in the literature to the best of the authors' knowledge but must also be investigated to fully understand erosion behavior of CMAS-exposed coatings. The erosion of brittle materials has been expressed as a removal of volume proportional to both target material and erodent properties [34,35]. One such model approximates volume loss V as:

$$V \propto U_k^{7/6} E_t^{5/4} K_{IC,t}^{-1} H_t^{-17/12} \quad (1)$$

where U_k is particle kinetic energy, E_t is target material elastic modulus, and $K_{IC,t}$ and H_t are the fracture toughness and hardness of the target material, respectively. This relationship developed by *Marshall et al.* has been shown to accurately model the erosion response of brittle monolithic materials, showing that material properties such as hardness and fracture toughness do have an effect on crack propagation during particle impingement. However, classical erosion models [36] do not account for defect centers such as porosity, unmelted particles, and lamellar cracks that would be present in plasma sprayed EBCs. Such defect centers can also form due to CMAS interactions and can affect mechanical properties.

Ultimately, erosion of CMAS-exposed EBCs is going to be a function of CMAS type, loading, temperature, and time (at temperature) and further work is needed to completely understand the governing mechanisms for erosion/CMAS synergies in EBCs. These results contribute to understanding

coupled effects of particle interactions in gas turbine engines and will be instrumental in developing future testing methodologies and predictive tools for EBC operating lifetimes.

4. CONCLUSIONS

The erosion durability of a modified $Yb_2Si_2O_7$ EBC was evaluated after exposure to low and high CMAS loads. Both the CMAS loading amount and heat treatment time had large effects on the thermomechanical durability of the coatings. Low CMAS loads and a shorter heat treatment time resulted in minimal change to erosion durability, although evidence of viscous sintering/densification due to the presence of the glass was observed. However, erosion durability at higher loads was more difficult to assess because of the tendency of erodent material to stick to residual CMAS on the coating surfaces. CMAS adhesion, extraneous phase formation as well as the formation of voids and cracks with higher loading meant that detrimental changes in the coatings were occurring may not necessarily be captured in cumulative mass loss plots. This study has shown that tracking changes in the chemistry and morphology of EBCs will be crucial in understanding the mechanisms of degradation due to high-temperature particle interactions.

ACKNOWLEDGEMENTS

The authors gratefully acknowledge Dr. Benjamin Kowalski and Dr. Kang Lee for thoughtful discussions and scientific input. This work was supported under the NASA Transformational Tools and Technologies (TTT) Project and the Hybrid Thermally Efficient Core (HyTEC) project.

REFERENCES

[1] Smialek, J. L., Robinson, R. C., Opila, E. J., Fox, D. S., and Jacobson, N. S., 1999, "SiC and Si3N4 Recession Due to SiO2 Scale Volatility under Combustor Conditions," Adv. Compos. Mater., **8**(1), pp. 33–45.

[2] Opila, E. J., Smialek, J. L., Robinson, R. C., Fox, D. S., and Jacobson, N. S., 1999, "SiC Recession Caused by SiO2 Scale Volatility under Combustion Conditions: II, Thermodynamics and Gaseous-Diffusion Model," J. Am. Ceram. Soc., **82**(7), pp. 1826–1834.

[3] Song, W., Lavallée, Y., Hess, K.-U., Kueppers, U., Cimarelli, C., and Dingwell, D. B., 2016, "Volcanic Ash Melting under Conditions Relevant to Ash Turbine Interactions," Nat. Commun., **7**(1), pp. 1–10.

[4] Webster, R. I., Bansal, N. P., Salem, J. A., Opila, E. J., and Wiesner, V. L., 2020, "Characterization of Thermochemical and Thermomechanical Properties of Eyjafjallajökull Volcanic Ash Glass," Coatings, **10**(2), p. 100.

[5] Wiesner, V. L., and Bansal, N. P., 2015, "Mechanical and Thermal Properties of Calcium–Magnesium Aluminosilicate (CMAS) Glass," J. Eur. Ceram. Soc., **35**(10), pp. 2907–2914.

[6] Presby, M. J., and Harder, B. J., 2021, "Solid Particle Erosion of a Plasma Spray – Physical Vapor Deposition Environmental Barrier Coating in a Combustion Environment," Ceram. Int., **47**(17), pp. 24403–24411.

[7] Lee, K. N., 2019, "Yb2Si2O7 Environmental Barrier Coatings with Reduced Bond Coat Oxidation Rates via Chemical Modifications for Long Life," J. Am. Ceram. Soc., **102**(3), pp. 1507–1521.

[8] Stokes, J. L., Harder, B. J., Wiesner, V. L., and Wolfe, D. E., 2021, "Melting and Crystallization Behavior of CaO-MgO-Al2O3-SiO2 Silicates Relevant to Turbine Engine Applications," NASA/TM-20210020388 https://ntrs.nasa.gov/citations/20210020388.

[9] Stokes, J. L., Harder, B. J., Wiesner, V. L., and Wolfe, D. E., 2019, "High-Temperature Thermochemical Interactions of Molten Silicates with Yb2Si2O7 and Y2Si2O7 Environmental Barrier Coating Materials," J. Eur. Ceram. Soc., **39**(15), pp. 5059–5067.

[10] Borom, M. P., Johnson, C. A., and Peluso, L. A., 1996, "Role of Environmental Deposits and Operating Surface Temperature in Spallation of Air Plasma Sprayed Thermal Barrier Coatings," Surf. Coatings Technol., **86**–**87**, pp. 116–126.

[11] Krämer, S., Yang, J., Levi, C. G., and Johnson, C. A., 2006, "Thermochemical Interaction of Thermal Barrier Coatings with Molten CaO-MgO-Al2O3-SiO2 (CMAS) Deposits," J. Am. Ceram. Soc., **89**(10), pp. 3167–3175.

[12] Harder, B. J., Stokes, J. L., Kowalski, B. A., Stuckner, J., and Setlock, J. A., 2023, "Steam Oxidation Performance of Environmental Barrier Coatings Exposed to CMAS."

[13] Kowalski, B., Stokes, J., Albert, P. E., Lauer, P. E., and Wolfe, D. E., 2023, "Effect of Test Parameters in the Exposure of Ca–Mg–Al–Silicate on Yttria Stabilized Zirconia," J. Am. Ceram. Soc., (January), pp. 1–11.

[14] Fox, D. S., Miller, R. A., Zhu, D., Perez, M., Cuy, M. D., and Robinson, R. C., 2011, "Mach 0.3 Burner Rig Facility at the NASA Glenn Materials Research Laboratory," NASA/TM--2011-216986 https://ntrs.nasa.gov/archive/nasa/casi.ntrs.nasa.gov/20110008403.pdf.

[15] Kuczmarski, M. A., Miller, R. A., and Zhu, D., 2011, "CFD-Guided Development of Test Rigs for Studying Erosion and Large-Particle Damage of Thermal Barrier Coatings," Model. Simul. Eng., **2011**.

[16] Miller, R. A., and Kuczmarski, M. A., 2013, "Burner Rig for Small Particle Erosion Testing of Thermal Barrier Coatings," J. Test. Eval., **42**(3).

[17] Miller, R. A., Kuczmarski, M. A., and Zhu, D., 2011, "Burner Rig With an Unattached Duct for Evaluating the Erosion Resistance of Thermal Barrier Coatings," NASA/TM-2011-217008 https://ntrs.nasa.gov/search.jsp?R=20110013364, (June).

[18] Bruce, R. W., 1998, "Development of 1232°C (2250°F) Erosion and Impact Tests for Thermal Barrier Coatings," Tribol. Trans., **41**(4), pp. 399–410.

[19] Presby, M. J., 2020, "Influence of Particle Velocity and Impingement Angle on Elevated Temperature Solid Particle Erosion of SiC/SiC Ceramic Matrix

Composite," NASA/TM-20205003560 https://ntrs.nasa.gov/citations/20205003560, (July).
[20] Ruff, A. W., and Ives, L. K., 1975, "Measurement of Solid Particle Velocity in Erosive Wear," Wear, **35**(1), pp. 195–199.
[21] Wiederhorn, S. M., and Hockey, B. J., 1983, "Effect of Material Parameters on the Erosion Resistance of Brittle Materials," J. Mater. Sci., **18**(3), pp. 766–780.
[22] Presby, M. J., 2021, "High-Temperature Solid Particle Erosion in a Melt-Infiltrated SiC/SiC Ceramic Matrix Composite," J. Eng. Gas Turbines Power, **143**(12), pp. 1–6.
[23] Stokes, J. L., Harder, B. J., Wiesner, V. L., and Wolfe, D. E., 2020, "Effects of Crystal Structure and Cation Size on Molten Silicate Reactivity with Environmental Barrier Coating Materials," J. Am. Ceram. Soc., **103**(1), pp. 622–634.
[24] Summers, W. D., Poerschke, D. L., Park, D., Shaw, J. H., Zok, F. W., and Levi, C. G., 2018, "Roles of Composition and Temperature in Silicate Deposit-Induced Recession of Yttrium Disilicate," Acta Mater., **160**, pp. 34–46.
[25] Godbole, E., Karthikeyan, N., and Poerschke, D., 2020, "Garnet Stability in the Al–Ca–Mg–Si–Y–O System with Implications for Reactions between TBCs, EBCs, and Silicate Deposits," J. Am. Ceram. Soc., **103**(9), pp. 5270–5282.
[26] Wiesner, V. L., Harder, B. J., Garg, A., and Bansal, N. P., 2020, "Molten Calcium–Magnesium–Aluminosilicate Interactions with Ytterbium Disilicate Environmental Barrier Coating," J. Mater. Res., **35**(17), pp. 2346–2357.
[27] Turcer, L. R., Krause, A. R., Garces, H. F., Zhang, L., and Padture, N. P., 2018, "Environmental-Barrier Coating Ceramics for Resistance against Attack by Molten Calcia-Magnesia-Aluminosilicate (CMAS) Glass: Part I, YAlO3 and γ-Y2Si2O7," J. Eur. Ceram. Soc., **38**(11), pp. 3905–3913.
[28] Turcer, L. R., Krause, A. R., Garces, H. F., Zhang, L., and Padture, N. P., 2018, "Environmental-Barrier Coating Ceramics for Resistance against Attack by Molten Calcia-Magnesia-Aluminosilicate (CMAS) Glass: Part II, β-Yb2Si2O7 and β-Sc2Si2O7," J. Eur. Ceram. Soc., **38**(11), pp. 3914–3924.
[29] Stokes, J. L., Bansal, N. P., and Wiesner, V. L., 2022, "Thermochemical Degradation of HfSiO4 by Molten CMAS," Ceram. Int., **48**(12), pp. 16499–16504.
[30] Miller, R. A., and Kuczmarski, M. A., 2015, "A CFD-Based Study of the Feasibility of Adapting an Erosion Burner Rig for Examining the Effect of CMAS Deposition/Corrosion on Environmental Barrier Coatings," NASA/TM--2015-218757 https://ntrs.nasa.gov/citations/20150018398, (August).
[31] Bansal, N. P., and Choi, S. R., 2015, "Properties of CMAS Glass from Desert Sand," Ceram. Int., **41**(3), pp. 3901–3909.
[32] Tromans, D., and Meech, J. A., 2004, "Fracture Toughness and Surface Energies of Covalent Minerals: Theoretical Estimates," Miner. Eng., **17**(1), pp. 1–15.
[33] Wang, J., Tian, Z., Zheng, L., Wang, J., Yang, J., and Yang, G., 2015, "Damage Tolerance and Extensive Plastic Deformation of β-Yb2Si2O7 from Room to High Temperatures," J. Am. Ceram. Soc., **98**(9), pp. 2843–2851.
[34] MARSHALL, D. B., LAWN, B. R., and EVANS, A. G., 1982, "Elastic/Plastic Indentation Damage in Ceramics: The Lateral Crack System," J. Am. Ceram. Soc., **65**(11), pp. 561–566.
[35] Aquaro, D., and Fontani, E., 2001, "Erosion of Ductile and Brittle Materials (Development of a FEM-Based Model and Its Assessment Against Theoretical Models and Experimental Data)," Meccanica, **36**, pp. 651–661.
[36] Hutchings, I., and Shipway, P., 2017, "Wear by Hard Particles," *Tribology*, Elsevier Ltd., pp. 165–236.